The dynamics of champagne cork popping revisited through high-speed schlieren imaging and computational fluid dynamics simulations

J. N. Fréreux, B. Tomasetti, A. Benidar, Gérard Liger-Belair, A. B. Himakar, M. P. Lakhan, R. P. Srikar, S. V. Nikhilesh, J. Gopalan, S. M. V. Rao, et al.

The dynamics of champagne cork popping revisited through high-speed schlieren imaging and computional fluid dynamics simulations

J. N. Fréreux,[1,2] B. Tomasetti,[1,2] A. Benidar,[3] G. Liger-Belair,[4] A. B. Himakar,[5] M. P. Lakhan,[5] R. P. Srikar,[5] S. V. Nikhilesh,[5] J. Gopalan,[5] S. M. V. Rao,[5] R. Georges,[3] and C. Lauzin[1]

[1)]*Institute of Condensed Matter and Nanosciences, Université catholique de Louvain, 1348 Louvain-la-Neuve, Belgium*

[2)]*Both authors contributed equally to this work and should both be considered as first author.*

[3)]*Institut de Physique de Rennes, UMR CNRS 6251, Université de Rennes, Campus de Beaulieu, 35042 Rennes Cedex, France*

[4)]*Groupe de Spectrométrie Moléculaire et Atmosphérique, UMR CNRS 7331, Université de Reims Champagne-Ardenne, 51687 Reims, France*

[5)]*Laboratory for Hypersonic and Shock wave Research, Indian Institute of Science, Bengaluru, Karnataka 560001, India*

(*robert.georges@univ-rennes1.fr)

(Dated: 10 April 2024)

The cork popping process present a rich and complex fluid dynamics. It involves up to three phases (liquid, gas and solid), three main chemical compounds (ethanol, water, CO_2) and a moving cork gradually opening the bottle and blocking the fast progression of the expanding gas. In this work, we used high-speed, high-sensitivity schlieren imaging setups to provide a fresh look on this dynamical phenomenon. Our experimental results are systematically compared and interpreted on the basis of new computational fluid dynamics (CFD) simulations. Our combined experimental and numerical works confirm the establishment of two supersonic expansions during the cork popping from a champagne bottle.

I. INTRODUCTION

From the physico-chemical point of view, champagne and other sparkling wines can be viewed as multicomponent hydroalcoholic solutions. They present a surface tension $\gamma \approx 50$ mN.m^{-1} (*i.e.*, reduced by about a third compared to that of pure water, mainly due to $\approx$ 12-13 % ethanol by volume), a viscosity close to 1.5 mPa.s ($\approx$ 50% more than that of pure water mainly because of ethanol), and a density relative to pure water close to unity[1]. Moreover, champagne and other sparkling wines are saturated with dissolved carbon dioxide (CO_2), whether during a second in-bottle alcoholic fermentation process for premium sparkling wines like champagne, or through simple exogenous gas-phase CO_2 injection for some cheaper sparkling wines[2]. For premium sparkling wines, the CO_2 produced by the yeasts during this second in-bottle fermentation cannot escape and progressively dissolves into the wine.

In a sealed bottle of sparkling wine, gas-phase CO_2 and dissolved CO_2 undergo thermodynamic equilibrium according to the so-called Henry's law. The concentration c_L of dissolved CO_2 in the wine is indeed proportional to the partial pressure of gas-phase CO_2, according to the formula $c_L = k_H P_{CO_2}$, with k_H being the strongly temperature-dependent Henry's constant of gas-phase CO_2 in wine[3], and P_{CO_2} being the partial pressure of gas-phase CO_2 in the sealed bottle. In addition, the temperature dependence of the Henry's constant leads to a strong temperature dependence of the pressure prevailing in the bottle hermetically sealed with a cork, as it was modeled by Liger-Belair *et al.*[4]. It goes from roughly 5 bars at 8 °C to more than 10 bars at 30 °C[4,5]. During the cork popping process, concomitantly with the cork stopper being expelled from the bottleneck under the action of CO_2 pressure, the underexpanded gas of the champagne bottle (mainly composed of CO_2 with traces of water vapor and ethanol) expands out of the bottleneck through the ambient air and experiences adiabatic cooling[4,5].

While free underexpanded jets are very well documented, for example see Franquet *et al.*[6], expansions which are obstructed are still challenging to rationalize[7–9]. In this respect, the cork popping of a champagne bottle is particularly interesting and challenging, as the position of the obstacle changes dynamically as the gas expands. Moreover, it involves up to three phases (gas, liquid and solid particles formed during severe adiabatic cooling), as well as a mixture of gases with different physico-chemical characteristics. This cork popping dynamics was recently studied using high-speed imaging[5]. Films were recorded for bottles stored at 20 and 30°C. These recordings allowed the observation of a planar shock wave (Mach disk) and of partial nucleation of H_2O and/or CO_2. The amplitude of this nucleation was different for the two temperatures and was deduced from the change of color following the major light scattering mechanism at play, *i.e.* Rayleigh or Mie scattering. This work initiated a numerical effort to better understand the details of the fluid dynamics[10]. A computational fluid dynamics (CFD) method was then used to simulate the expansion of 7.5 bar of pure CO_2 obstructed by a rigid cork moving at a constant speed. The authors, most of them involved in this work, computed dynamically the Mach number, temperature, pressure and density of the expanding gas with a time resolution of 1 µs. The simulation predicted the apparition of a complex set of radial shock waves at early time of the expansion. The experimental observation of a planar shock wave going

first towards the cork and later, when the bottle pressure decreased, towards the bottle was also reproduced by the modeling. Diamond-shaped cells expanding radially from the compressed gas impacting the cork were predicted but not observed experimentally. In this work, we use high-speed schlieren imaging combined with new CFD simulations to provide a new look on this interesting phenomenon.

The article is organized as follows: the physical characteristics of typical champagne bottles are presented in section II A. The improvements of the CFD simulations compared to the work of Benidar *et al.*[10] are provided in II B. The experimental setups and procedures are presented in section II C. The results of the CFD simulations are described in section III A before to present the experimental results obtained through high-speed schlieren imaging in section III B. Finally, conclusions and perspectives are discussed in the last section of this manuscript.

II. MATERIALS AND METHODS

A. Presentation of physical parameters of a typical champagne bottle

Experimentally, a series of 75 cL bottles obtained from different suppliers were used. Typically, champagne bottles present 12-13% ethanol by volume concentration. To trigger the second in-bottle alcoholic fermentation needed to force the dissolution of gaseous CO_2 in these bottles (the so-called *prise de mousse*), yeasts along with 20 to 24 g.L^{-1} of sugar were classically added in the bottles hermetically sealed. The key metabolic process behind the production of gas-phase CO_2 in the sealed bottles is alcoholic fermentation. Actually, 20 to 24 g.L^{-1} of sugar added in the blend leads to the production of 7.3 to 8.8 g of CO_2 (*i.e.*, $\approx$ 0.17 to 0.2 mol) in every bottle of champagne[4]. After the *prise de mousse* was achieved, bottles are aged in a cool cellar for at least 15 months. Bottles are then disgorged, which consists in opening the bottles to remove the dead yeast cells and recorking them with traditional natural cork stopper. During this step, the thermodynamic equilibrium of CO_2 is broken, but dissolved and gas-phase CO_2 quickly recover Henry's equilibrium in the recorked bottle where a volume V_G of gas phase (the headspace) still cohabits with a volume V_L of champagne (*i.e.*., the liquid phase). It is worth noting that, into every bottle of a batch, the volume V_G of the headspace under the cork is 25-35 mL, whereas the volume V_L of champagne is 75 cL. Recently, the pressure-temperature relationship in the corked bottles (after the disgorging step was achieved) was theoretically determined[4]. It obeys the following relationship, with every parameter being expressed in the international system of units (SI):

$$P^{CO_2} = \frac{n k_H (RT)^2 V_L}{(V_G + n k_H RT V_L)^2} \quad (1)$$

with P^{CO_2} being the CO_2 pressure in the corked bottle, n being the total number of CO_2 moles produced in a sealed bottle after the *prise de mousse* (*i.e.*, 0.17 to 0.2 mol in the present case), k_H being the temperature-dependent Henry's constant of gas-phase CO_2 in wine[3], R being the ideal gas constant, and T being the temperature. Thermodynamically speaking, the temperature-dependent Henry's constant of gas-phase CO_2 in wine was found to be conveniently expressed with a Van't Hoff like equation as follows[3]:

$$k_H(T) = k_{298K} \exp\left[-\frac{\Delta H_{diss}}{R}\left(\frac{1}{T} - \frac{1}{298}\right)\right] \quad (2)$$

with k_{298K} being the Henry's constant of CO_2 at 25 °C ($\approx$ 1.2 g.L^{-1}.bar^{-1}, *i.e.*, 2.7×10^{-4} mol.m^{-3}.Pa^{-1}), and ΔH_{diss} being the dissolution enthalpy of CO_2 in wine ($\approx$ - 24 800 J.mol^{-1}). For the standard commercial champagne bottles of the present study, applying equation (1) leads to CO_2 pressures ranging between 7.4 and 8.9 bars in the corked bottles stored at 25 °C.

B. CFD calculations

Our numerical simulations represent an extension of a prior investigation as documented in Benidar *et al.*[10]. We recommend referring to our initial publication for comprehensive details on the basic framework and associated assumptions. Briefly, all the simulations are based on the use of the commercial solver ANSYS Fluent. These simulations are conducted under the assumption of axisymmetric geometry. The standard k-epsilon turbulence model is employed with a near-wall treatment. This turbulent model was implemented in order to deal with the large velocity fluctuations in the region of the radial expansion and in the shear layers of the axial expansion (colormaps of turbulence intensity are available in supplementary materials, Fig. S1). The k-ε Reynolds-Averaged Navier-Stokes (RANS) model is preferred to more elaborate models dedicated to the dynamic interactions of fluids around the moving object (such as the Unsteady RANS model), in order to balance accuracy and computational feasibility. While this approach may not capture all the transient effects, it provides a reasonable approximation of the flow behavior and allows us to obtain valuable insights within the constraints of our computational resources.

For simplicity, we assume that the gas contained in the bottle is composed exclusively of CO_2. Initial conditions are defined with a 35 mL headspace, a pressure of 7.5 bar and a temperature of 20°C. The external gas is air at 20°C and atmospheric pressure. According to current and past experimental observations[4,5], no net variation in cork velocity was observed after $\sim$100 µs and thus for most of the duration of supersonic expansions. Consequently, the cork velocity is fixed as a constant (18.6 m.s^{-1}) in the numerical simulations. A CAD (computer-aided design) file of a real champagne bottle was used to define the bottle profile. Moreover, it is assumed that the cork geometry is not modified during the process. This assumption simplifies the simulation and is realistic for old champagne bottles. Indeed after 12 years of age, a natural cork stopper deforms less and tends to keep a cylindrical shape whose diameter correspond to that of the

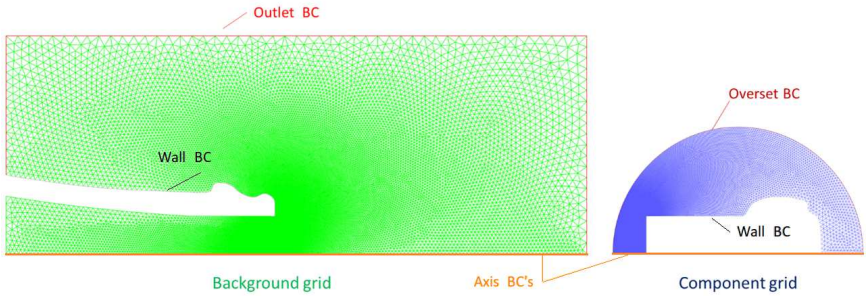

FIG. 1: Overset mesh and boundary conditions (BC). Two distinct computational domains are defined: the background domain (length × width: 160 × 45 mm^2) and the overset domain (radius: 30 mm).

bottle neck[11] (more information available in the supplementary materials). For a detailed study of cork deformation during uncorking and its consequences on the gas dynamics, readers should refer to Wagner, Braun, and Scheichl[12].

The quality of the CFD simulations compared to our previous study[10] was improved by enhancing the spatial and temporal resolution. This was performed by decreasing the calculation time step from 1 µs to 50 ns and by changing our meshing strategy. To ensure precise predictions of the flow field, it is indeed imperative to provide an adequate grid density in the mixing region. This includes sufficient grid density to capture high-velocity gradient regions within the shear layer and a large number of grid elements to resolve high-pressure gradient regions near shock fronts. In our prior study, which employed a dynamic meshing technique, grid density in the mixing region proved highly sensitive to dynamic layering, smoothing, and remeshing techniques. The efforts to refine the mesh in a specific flow region often resulted in calculation divergence.

In these revised numerical simulations, we have adopted an overset meshing method[13,14] capable of accommodating moving bodies within turbulent flows. Unlike the previous approach that involved sliding meshes, mesh morphing, and remeshing, this alternative mesh handling strategy creates separate grids that overlap instead of being complementary. Each component is treated as an independent body with its dedicated grid. The overset method simultaneously computes all grids, encompassing the component zones and background zones. Field variables are interpolated from all grids at each time step. This approach mitigates computational complexity and ensures realistic motion simulations for complex geometries. As previously mentioned, the computational domain is divided into two parts: an overset mesh comprising the moving cork and the surrounding fluid, and a background mesh used to model the static bottle and its surrounding fluid, as depicted in Fig. 1. In both domains, the meshing is variable, ranging from 0.001 mm for the finer mesh to 1 mm for the coarser mesh. Cell zone conditions are specified with a fixed mesh for the background grid and a moving mesh for the component grid, featuring a translational velocity of 18.6 m/s. Boundary conditions for walls are set as stationary for the bottle and as moving for the cork with a velocity of 18.6 m/s . Shear conditions for all walls are defined as non-slip.

C. Experimental apparatus

Two experimental setups were used in this work, one located at UClouvain (Louvain-la-Neuve, Belgium) and the other at the Laboratory for Hypersonic and Shock wave Research (Bangalore, India). These setups will be named hereafter UCLouvain and LHSR, respectively. The general scheme of the two setups is the same and is presented in Fig. 2. This corresponds to a z-type parallel-light schlieren system[15–18]. In UCLouvain, a halogen lamp is used in combination with a short focal lens and a diaphragm of 3 mm diameter to produce a point (white) light source (LS). This point source is placed at the focal point of a first spherical mirror (SM1) (D_1 = 0.46 m, f_1 = 5 m). The resulting collimated beam passes through the studied area and a second spherical mirror (SM2) (D_2 = 0.70 m, f_2= 3.5 m), placed 2.6 m after the studied area, images the light beam source on its focal point where a spatial filter is placed. Light transmitted by the spatial filter is recorded by a camera (HighSpeedStar 3G, LaVision). Camera recording parameters are set to 20,000 frames.s^{-1} with a 512 x 128 pixel matrix (8-bit grey scale) and 50 µs exposure time.

In LHSR, the two mirrors have focal lengths of f_1 = f_2 = 3 m and diameters of D_1 = D_2 = 280 mm. The light source is a high power LED (operated at 40 W) emitting continuous light at 532 nm. The camera used for the acquisition is a Photron Fastcam SA4, recording 512 x 304 pixels images at a rate of 22,500 frames per second and 3.25 µs exposure time. For all measurements presented in this work, spatial filtering was performed using a razor blade (RB) knife-edge in order to maximize the contrast on supersonic patterns. The spatial filtering was performed vertically, *i.e.* the blade is placed

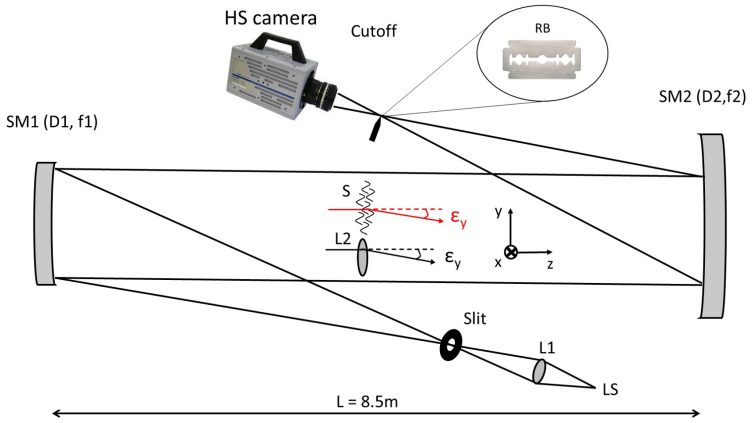

FIG. 2: Schematic of the parallel-light z-type schlieren setup. SM stands for spherical mirrors, D for diameter, f for focal length and LS for light source. S for sample and ε for light deviation.

along the x axis, since the vertical axis y is the axis of the expansion (bottom part of light spot is cut by the RB).

In UCLouvain, a lens (L2 in Fig. 2) with a long focal length of f = +10 m is placed a few centimeters from the studied area and allows the quantification of the total deviation angle of the light[17] as detailed in the supplementary material (Fig. S1). Using this calibration, a minimum measurable deviation was evaluated to be 0.4 arcsecond (100 µdegree) at a distance of 6.1 m between the lens and the RB. Total light deviation can be used to quantify local thermodynamic variations[19–22]. The estimation of the total deviation is additional information given by our studies but is not developed in this paper. All the figures presented in this work are from two measurement campaigns carried out at UCLouvain in December 2022 and June 2023, with the exception of the results presented in Fig. 4 associated with measurements carried out at LHSR in November 2022. For measurements done at UCLouvain, the champagne and sparkling wine bottles were placed and maintained at a given temperature either using a bain-marie and a heating plate or using a heating tape and a PID device to reach a reference temperature.

III. RESULTS AND DISCUSSION

The results of the CFD simulation (Fig. 3) and those of the experiments carried out at LHSR and UC Louvain (Figs. 4 and 5 respectively) have multimedia content available (multimedia view).

A. CFD simulations results

The CFD predictions of the flow density evolution are presented in Figure 3. The full animation is also available (multimedia view). This dynamics can be arbitrarily divided in three stages for times ranging from 0 to 1.5 ms, where $t = 0$ is defined as the frame before the appearance of exiting gases. The first stage of the popping process is illustrated in panel a) of Fig. 3. A radial expansion through the thin annular gap is created when the cork begins to separate from the bottle. An expansion zone (rarefaction fan), typical of free underexpanded jets, forms at the edges of the bottleneck, and Mach number simulation (not shown) reveals that the gas has already acquired supersonic radial velocity.

The second stage is illustrated in panels b and c) of Fig. 3. The gas expansion just above the bottleneck becomes an axial jet whereas the start of radial jet remains located at the base of the cork. Mach number simulation (not shown) reveals that the axial expansion is also supersonic. However, the cork clearly compresses the impinging gas and therefore this expansion can be defined as an impinging supersonic jet[8,23–27]. The formation of a first Mach disk is predicted as a sudden change of density is observed when the gas flows from the axial expansion to the compression zone under the cork. In this regime, the impinging gas maintains a sufficiently high pressure ratio in the compression zone compared with atmospheric pressure: the radial jet remains supersonic, as shown by the succession of diamond shock cells. Therefore, the gas flow from the bottle undergoes two distinct supersonic expansions: first, an axial impinging supersonic expansion at the bottle exit, followed by a compression of the gas due to presence of the cork and, second, a re-acceleration to supersonic speed during the radial free expansion. The distance of the Mach disk from the bottle increases as the

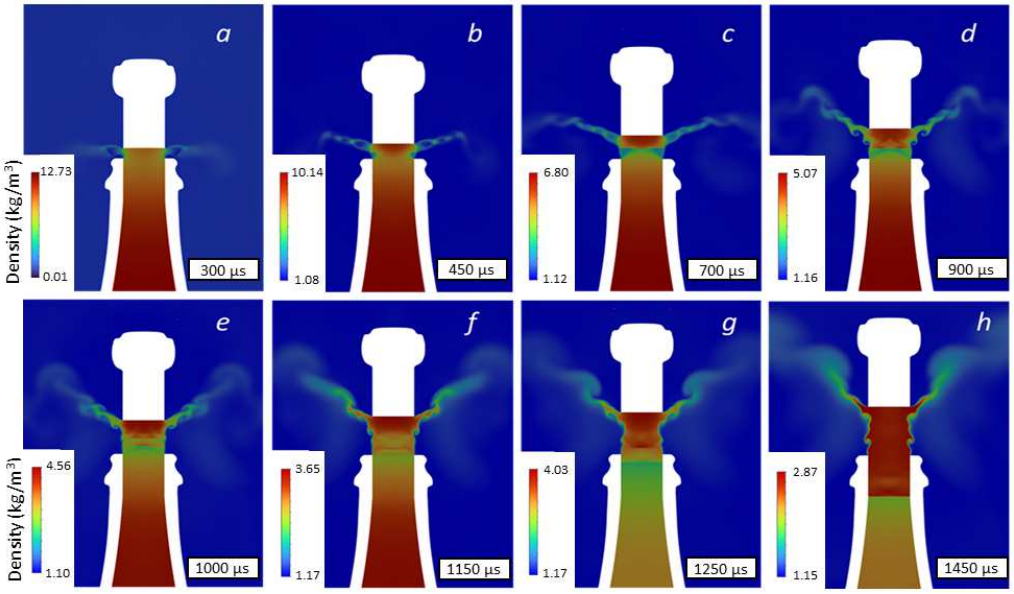

FIG. 3: CFD simulation of the 2D axisymmetric density profile for the cork popping process using the overset meshing method (multimedia view). Initial parameters are: headspace gas volume = 35 mL, pressure = 7.5 bar and temperature = 20°C. The gas in the bottle is pure CO_2 and the surrounding gas is air. A variable density scale is used to enhance the contrast of the fluid dynamics features. The same figure with a fixed scale is provided in the supplementary materials.

standoff distance between the cork and the bottle increases, and reaches a maximum that defines the ends of stage no. 2. In our previous CFD simulation[10], the impact of the cork on the position of the Mach disk was described, emphasizing the impinging nature of the axial expansion.

The third stage associated to t $\geq$ 800 µs is presented in panels d to h) of Fig. 3. The pressure ratio between the compression zone under the cork and the bottle drops below a critical point where the extension of the axial supersonic expansion cannot be sustained. The Mach disk formed by the axial expansion appears to fall back to the bottle[28,29]. During the collapse of this first Mach disk, a second Mach disk is created further downstream of the axial expansion (*i.e.* at a larger distance from the bottleneck). At later time this second disk appears to follow the first one by collapsing towards the bottle. The second Mach disk (Fig. 3, panel e) is delimiting the end of the second shock cell. It should be noted that the drop in bottle pressure leads to a continuous decrease in the pressure ratio, which shortens the shock cells and moves the Mach disks towards the bottleneck[7,8]. At the same time, the supersonic character of the radial expansion is lost, as the pressure under the cork is no longer sufficient to sustain it. Finally, instabilities are developing in the boundary layers of the jet (vortices) and a compression wave propagates inside the bottle (Fig. 3, panel h).

The improvement of the temporal and spatial resolution of the CFD simulations allowed to provide new information. Especially the appearance of a second Mach disk during the collapse stage is a new feature directly associated to these improvements. This pattern was also numerically predicted recently in Wagner, Braun, and Scheichl[12]. A possible limitation of this CFD model can also be mentioned. In panels d) and e) of Figure 3, the simulations predict the appearance of large vortices in the radial expansion after the loss of its supersonic character. However, as we shall see in the next section, these vortex-like structures have not been observed experimentally so far and may be numerical artifacts. It should be mentioned, that the presence of vortex-like structures is only indicative in schlieren images, which is limited by line-of-sight integration effects and camera spatial resolution. Improvements in experimental spatial resolution and combination with other types of measurement, such as particle image velocimetry, would be required to observe such features.

B. High-speed schlieren imaging of a cork popping off a champagne bottle

Experimentally, our first objective was to confirm using schlieren imaging the presence of the normal shock wave (Mach disk) first observed by visible light scattering by Liger-Belair *et al.*[5] and subsequently confirmed by numerical simulations[10,12]. The LHSR experimental setup was used to visualize gas ejection from the head volume of a bottle of sparkling wine held at 25°C. Fig. 4 shows a chronological sequence of selected images filmed at the LHSR; the complete film is available (multimedia view), t = 0 is defined as (previously) the frame before the appearance of exiting gases. The film clearly reveals the formation of a Mach disk (MD1) around 711 µs after the cork separates from the bottle (remember here that the time interval between two images is 44.4 µs, so MD1 could in fact have appeared earlier in a 44.4 µs time interval). This observation is nicely confirming the supersonic nature of the axial gas expansion and the relevance of the numerical simulations in Benidar *et al.* [10] and in Wagner, Braun, and Scheichl [12]. MD1 then rises steadily above the bottle, before suddenly deepening towards the bottle at around 1289 µs as predicted in numerical simulations. A second Mach disk (MD2) forms downstream of MD1 at 1422 µs, slightly beyond the highest position ever reached by MD1 and then falls toward the bottle as predicted by the CFD simulation. This is the first experimental observation of the formation of this second mach disk in cork popping process. At 1511 µs, MD1 disappears into the bottleneck, followed by MD2 at 1600 µs. The graph in the last panel of Fig. 4 shows the temporal evolution of the position of MD1 and MD2, as well as the base of the cork relative to the bottleneck. The splitting of points at short times are associated to the observation of a thick disk instead of a line at early times of the expansion : each series of points is associated to the maximum and minimum height of this disk respectively.

A second measurement campaign was carried out at UCLouvain, during which new fluid dynamics phenomena were revealed. Specific frames of the dynamics of a champagne popping during this latter campaign are displayed in Fig. 5 (multimedia view). The time, t, associated to each panel is indicated in the lower left side. This was recorded with a frame rate of 20,000 fps, *i.e.* $\Delta t = 50$ µs time resolution. Once again, t = 0 is defined as the frame before the appearance of exiting gases. The velocity of the expelled cork is rapidly increasing reaching a value of 17 m/s after t = 150 µs, a value similar than the one obtained in previous studies[5]. Similar to the results above, the rise and fall of the horizontal Mach disk was again observed (see 600, 750, 900 µs in Fig. 5). However, the characteristic times associated with this process are clearly different as the maximum stretch of Mach disk 1 was occurring 1200 µs after the first appearance of gas in Fig. 4, whereas the global supersonic dynamics is already finished at that time in Fig. 5. This time dispersion was already observed previously[5] and is characteristic of changes in thermodynamic conditions and in particular changes in temperature. Nevertheless, despite this time dispersion, the fluid dynamics features predicted by CFD calculations were observed in these films.

Fluid dynamics of the cork popping process evolves rapidly over time. At early times, *e.g.* at t = 300, 450, 600 and 750 µs, lateral diamond shock cells are clearly visible. The origin of these structures is located at the basis of the cork and follows its movement. These structures were predicted by CFD modeling[10,12] but were so far never observed experimentally. This new experimental observation is confirming the formation of a radial free supersonic jet as discussed in section III A. This lateral shock cells feature remains clearly visible despite the latter formation of a Mach disk (*e.g.* t = 600 and 750 µs) through which the axial flow at the bottle outlet becomes subsonic close to the cork. An interesting frame is the one at t = 750 µs. This frame is reproduced in Fig. 6 with a comparison with CFD simulation of the spatial distribution of the Mach number. The comparison is not direct but illustrative since it presents two different quantities, the Mach number (CFD simulation) for the upper panel and the density gradient along the y axis for the lower panel (schlieren image). In the simulation, the color codes clearly indicates subsonic (white to black) and supersonic (green to red) regions. Five zones are highlighted in the experimental image and discussed in detail below.

In zone 5, the above-mentioned radial expansion is clearly visible through periodic pattern of alternating dark and bright areas on both sides of the expansion. This regular pattern develops very early in the process, at $t = 150 - 200$ µs, and is characteristic in schlieren imaging of a diamond structure originating from underexpanded supersonic jets[30–32]. Diamond-shaped cells are observed at the start of the expansion stage and last until t = 800 µs, when the cork is 1 cm above the bottle neck (see Fig. 5 at 750 µs). The observation of diamond-shaped shock cells at this later stage requires the presence of a high-pressure gas just under the cork (zone 4 in Fig. 6). This is in line with the expansion scheme described above in section III A where a high-pressure zone under the cork is formed. In addition, as observed in the experimental image, the radial deformation of the cork is very limited. Our numerical simulations, assuming a non-deforming cork, are able to reproduce the deflection angle of the radial expansion. Interestingly, this angle of deflection is much more pronounced in the images in Fig. 4 with a clear expansion of the cork once the bottle is fully open. This deformation was taken into account in the simulations carried out by Wagner, Braun, and Scheichl [12] (see Fig. S8) with a mentioned relation between the radial expansion of the cork during the opening and the large deflection angle of the radial expansion. This is thus confirmed by our observations.

Zone 3 highlights a thin horizontal feature located respectively upstream of zone 4 and downstream of zone 1. A similar feature is observed in high-speed direct color imaging[5]. This feature was also predicted in our simulations and in Wagner, Braun, and Scheichl [12] and is assigned to the formation of a horizontal Mach disk.

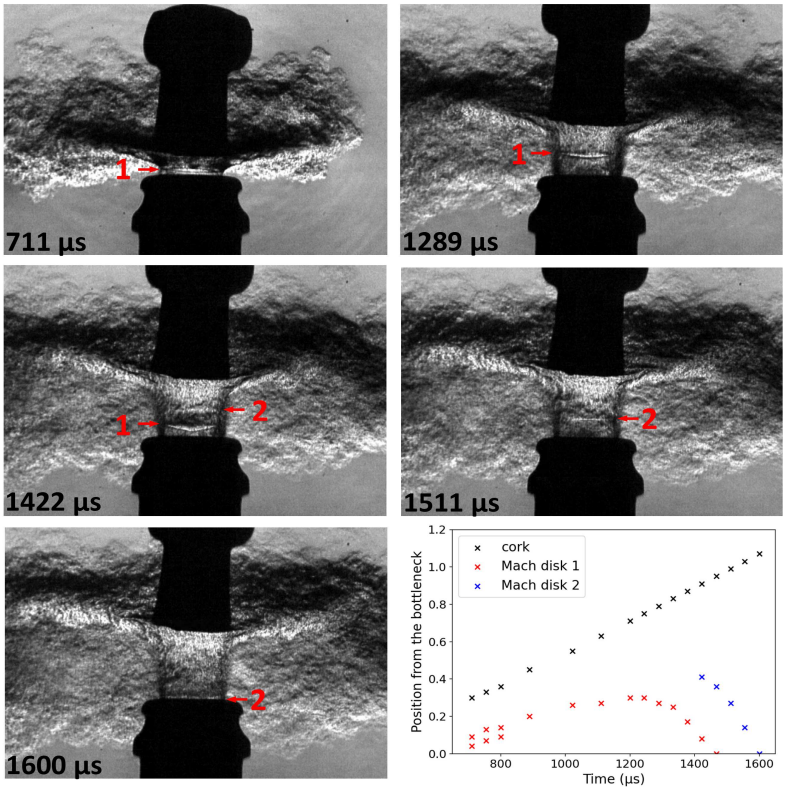

FIG. 4: Time sequence showing the cork popping process of a champagne bottle at 25°C at LHSR in Bangalore, India (multimedia view). The times shown on the frames correspond to the times elapsed after the first appearance of gas. The spatial filtering was performed using a RB placed horizontally. The last panel shows the positions of the cork (black), the Mach disk 1 (red) and Mach disk 2 (blue) versus time. Positions are expressed in diameter of the bottleneck.

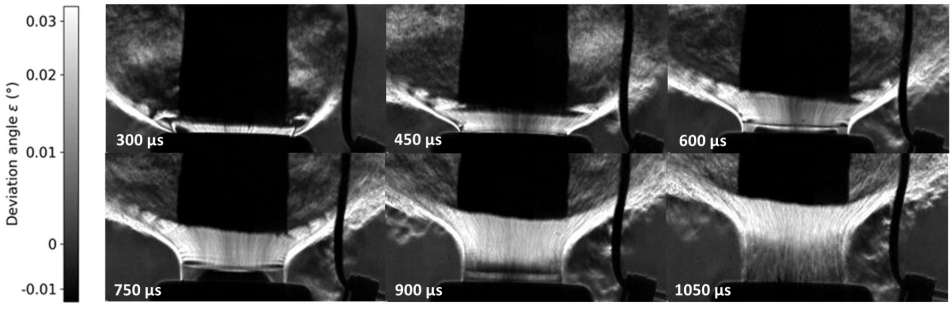

FIG. 5: Time sequence showing the cork popping process of a champagne bottle at 25°C in UCLouvain, Belgium (multimedia view). The time of each frame is indicated in the lower left. The spatial filtering was performed using a razor blade placed horizontally.

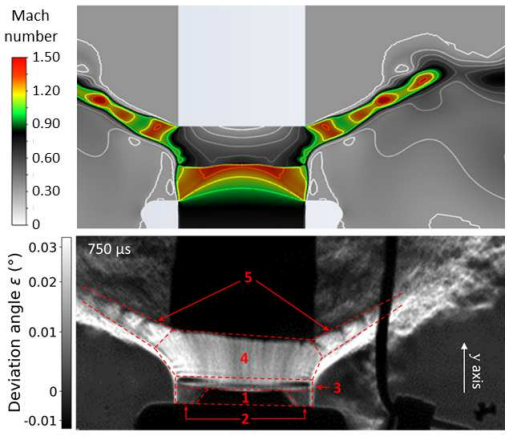

FIG. 6: Upper panel: Mach number map resulting from CFD simulation. Shades of grey are reserved for subsonic regions and color are reserved to supersonic regions. Solid green line is representing the sonic line. Bottom panel: schlieren image at 750 µs after the gas has escaped from the bottle. Expansion zones discussed in the text are highlighted and labeled in red. Refractive index gradients are observed along the y axis.

The dark zone 1 shown in Fig. 6 is located upstream of the first Mach disk. Zone 1 has an important contrast with the surrounding area (zone 2 in Fig. 6). This is an indicator of an edge in gas density variation. In this experimental measurement, the spatial filtering (*i.e.* the razor blade) is cutting the bottom part of the light spot. Therefore, dark areas in our images correspond to negative gradient of the refractive index (and thus of density) along the y axis (see supplementary Fig. S4). As zone 1 is appearing black in our images, zone 1 is a higher pressure area when comparing to zone 2 so we assigned zone 1 to the subsonic part of the expansion and zone 2 to the supersonic zone. This pure experimental assignment is in agreement with the CFD maps shown in Fig. 6. In these CFD map, a convex sonic line is expected and the axial extension of the supersonic area is maximized on side of the expansion and not on the central axis. Convex shape of the subsonic area at the exit of the nozzle is commonly observed in supersonic expansions[33,34]. Experimental observation of the features corresponding to zone 1 and 3 (Mach disk) confirms the supersonic nature of the axial expansion.

In zone 4, the compression zone shows alternating light to dark horizontal ripples just above zone 3. These ripples look blurry in Fig. 6 but they are clearly visible in the video (multimedia view). These ripples appear over time as the main Mach disk rises. The number of oscillations increases over time until they disappear completely very shortly (1 frame or around 50 µs) after the main Mach disk begins to descend towards the bottleneck. Therefore, the presence of these ripples seems to be strongly linked to that of the main Mach disk. On the CFD map dedicated to Mach number in Fig. 6, small supersonic cells are computed on side of the compression zone. The supersonic cells are in fact ring-shaped and are probably responsible for the observation of these ripples in the experimental image. These ring-shaped supersonic cells were predicted neither in our previous CFD[10] nor in reference Wagner, Braun, and Scheichl[12]. However, our updated calculation method now allows us to predict similar structures which could be related to reflections of compression waves after the Mach disk. A viscous instability could be another explanation, which would explain why our CFD simulations that include viscosity manage to partially reproduce these periodic structures, whereas the simulations in Wagner, Braun, and Scheichl[12] that neglect viscosity do not. A more detailed comparison between the experiment and the simulations about this zone 4 can be found in supplementary Fig. S5.

The time-dependent positions of the cork and the first Mach disk measured in the present work are compared in Fig. 7 with those observed and calculated in previous works[5,12]. Time t = 0 is defined as the time corresponding to a distance of +3.5 mm between cork and bottle. This arbitrary time reference is used to reduce the temporal dispersion of data, which is particularly pronounced for the experimental ones. This definition of t = 0 allows the time reference to be set in the time domain where the cork motion is linear, so that the time reference no longer depends on the complex early dynamics of the cork. In this figure, the colored curves and symbols correspond to the Mach disk positions, while the black curves and symbols correspond to the positions of the cork. Symbols refer to experimental data, while solid lines refer to numerical simulations. For the sake of clarity, the existing data are divided in two different panels, but the data of the left panel are reproduced on the right panel in light grey for comparison purposes. When examining Fig. 7, readers should consider the frame rate of experimental data as an indication of their uncertainties over time (Δt = 44, 50 and 83 µs for LHSR, UCLouvain and Liger-Belair et al. 2019 studies respectively).

Fig. 7 clearly shows that the cork reaches a constant speed around 100 µs after opening. This figure also highlights the experimental reproducibility of the time evolution of the first Mach disk, particularly before the Mach disk reaches its maximum distance value. Larger deviations are observed when focusing on the maximum height, which corresponds to the beginning of the last stage (expansion collapse stage). They probably result from variations in initial thermodynamic conditions (pressure, temperature, composition of the gas/champagne). No straightforward relationship between cork speed and maximum Mach disk height could be established: compared with UCLouvain measurements, the cork speed at LHSR is slightly slower, while the maximum Mach disk height is greater. The CFD simulation presented in this work is also shown in Fig. 7 (continuous blue curve), and

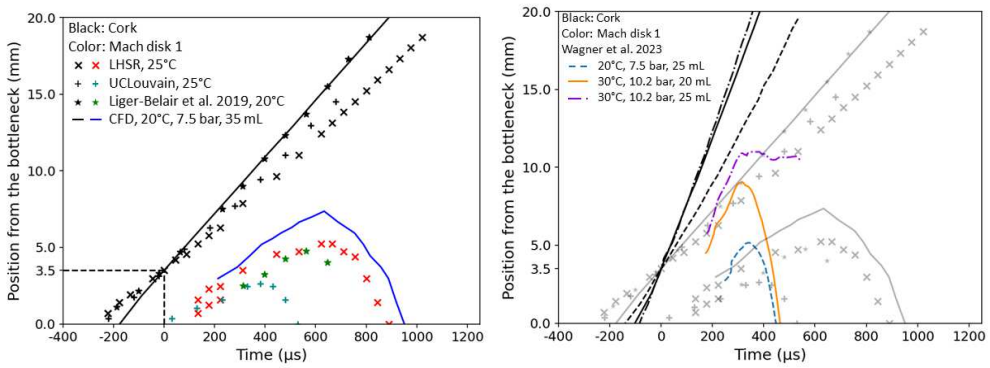

FIG. 7: Time evolution of the positions of the cork (in black) and the first Mach disk (in color). LHSR, UCLouvain and CFD refer to videos related to Figs. 4, 5 and 3 respectively. Liger-Belair et al. 2019 are data reproduced from standard high-speed imaging[5]. Wagner et al. 2023 are data reproduced from earlier numerical simulations[12]. The data presented in the left panel are reproduced in grey in the right panel. Initial thermodynamic conditions are indicated when available.

correctly reproduces the global evolution of the Mach disk. The recent full fluid-structure interaction model including the friction of the cork in the bottle[12] is also compared to our results in the right panel of Fig. 7. This model shows greater disagreement with our experimental observations. The systematic overestimation of the cork speed could be the reason for the faster time evolution of the Mach disk.

Finally, beside the supersonic dynamics described above, damped periodic gas breathing was observed with a frequency of ∼600-1000 Hz for large times > 2 ms (see video UCLouvain, multimedia view). This damped periodic oscillation at the bottleneck outlet has already been observed in previous works[4,5]. This observation is in agreement with previous simulations[10,12] where a compression wave propagates in the bottle on this large time scale. According to these simulations, Mach disks 1 and 2 convert into a compression wave that propagates back in the bottle. This compression wave is reflected by the liquid surface and at the bottleneck outlet (due to acoustic impedance mismatch). Gas dynamics at the bottleneck outlet over a long period was simulated by Wagner, Braun, and Scheichl [12] and an oscillation period of ∼1 ms was calculated. This oscillation period concurs with our observation.

IV. CONCLUSIONS AND PERSPECTIVES

In this study, an extensive characterisation of the rich fluid dynamics following the uncorking of a bottle of champagne was carried out. Based on CFD calculation relying on the overset meshing method, two types of supersonic expansions were predicted: an impinging supersonic expansion along the symmetry axis of the bottle and a free radial supersonic expansion on side of the cork. High-speed schlieren imaging has been used to test the qualitative validity of these predictions. The presence of diamond shock cells in the radial gas expansion zone was observed experimentally for the first time, confirming the supersonic nature of the deflected jet. The supersonic nature of the axial expansion is also confirmed by identifying the supersonic and subsonic zones of this expansion, in agreement with the CFD calculations. Beyond the confirmation of the two supersonic expansions, formation of a second Mach disk during the collapse of the supersonic expansion has been revealed by schlieren imaging. This second Mach disk was predicted in our new CFD simulations and was predicted in a recent work[12] but was never observed experimentally. In addition, horizontal ripples in the outer part of the deflected jet were observed but not predicted in any previous CFD calculation. In parallel to this work some of us have evidenced aggregation from an expansion of a mixture of CO_2 and H_2O[5,35]. To evidence such molecular mechanisms in real time would provide a fresh perspective on this interesting process.

V. SUPPLEMENTARY MATERIAL

See the supplementary material for additional results and explanations. Figure S1: Illustration of the flow turbulence; Figure S2: Ageing of champagne corks; Figure S3: Calibration of the deviation angles in schlieren imaging; Figure S4: Ray tracing for a high-density zone in an axially symmetric expansion; Figure S5: Figure 3 with a common density scale; Figure S6: Presentation of a reference cork launcher; Figure S7: Schlieren images using the reference cork launcher; Figure S8: Qualitative comparison between observed and simulated ripples.

ACKNOWLEDGMENTS

The authors acknowledge the financial support by the Fédération Wallonie Bruxelles, through the project "iBEAM" funded by its research program "Actions de Recherche Concertées" (convention no. 18/23-090) and the FNRS for a "mandat d'impulsion scientifique" (MIS, grant No F.4038.24). B.T. is a research fellow (ASP) of the FNRS. Authors also acknowledge the Institute of Mechanics, Materials, and Civil Engineering of UCLouvain for its technical support. The Castelanu Champagne producer is warmly acknowledged for providing bottles used in one of the measurement campaign.

VI. AUTHOR CONTRIBUTIONS

* Experimental results obtained at UCLouvain were conducted by J. N. Fréreux, B. Tomasetti and C. Lauzin. Experimental results obtained at LHSR were conducted by A. B. Himaka, M. P. Lakhan, R. P. Srikar, S. V. Nikhilesh, J. Gopalan, S. M. V. Rao. CFD simulations were performed by A. Benidar. G. Liger-Belair is the champagne physicist who supervised the link between the experimental conditions and the simulations. Robert Georges and Clément Lauzin both supervised the entire work. They, equally, contributed to the interpretation of the results and the formatting of the manuscript. J. N. Fréreux and B. Tomasetti should be both considered as first author.

[1]G. Liger-Belair and C. Cilindre, "Recent progress in the analytical chemistry of champagne and sparkling wines," Annual Review of Analytical Chemistry **14**, 21–46 (2021).
[2]C. Gonzalez Viejo, D. D. Torrico, F. R. Dunshea, and S. Fuentes, "Bubbles, foam formation, stability and consumer perception of carbonated drinks: A review of current, new and emerging technologies for rapid assessment and control," Foods **8**, 596 (2019).
[3]G. Liger-Belair, "Effervescence in champagne and sparkling wines: From grape harvest to bubble rise," The European Physical Journal Special Topics **226**, 3–116 (2017).
[4]G. Liger-Belair, D. Cordier, J. Honvault, and C. Cilindre, "Unveiling co2 heterogeneous freezing plumes during champagne cork popping," Scientific Reports **7**, 10938 (2017).
[5]G. Liger-Belair, D. Cordier, and R. Georges, "Under-expanded supersonic co2 freezing jets during champagne cork popping," Science advances **5**, eaav5528 (2019).
[6]E. Franquet, V. Perrier, S. Gibout, and P. Bruel, "Free underexpanded jets in a quiescent medium: A review," Progress in Aerospace Sciences **77**, 25–53 (2015).
[7]A. Sinha and I. V. L. N. Parasuram, "Underexpanded jet impingement on a plane wall—effect of npr and jet standoff distance," in *Fluid Mechanics and Fluid Power (Vol. 3)*, edited by S. Bhattacharyya, S. Verma, and A. R. Harikrishnan (Springer Nature Singapore, Singapore, 2023) pp. 13–18.
[8]J. Wilkes Inman, P. Danehy, R. Nowak, and D. Alderfer, "Fluorescence imaging study of impinging underexpanded jets," in *46th AIAA Aerospace Sciences Meeting and Exhibit* (2008) p. 619.
[9]F. Alvi, J. Ladd, and W. Bower, "Experimental and computational investigation of supersonic impinging jets," AIAA journal **40**, 599–609 (2002).
[10]A. Benidar, R. Georges, V. Kulkarni, D. Cordier, and G. Liger-Belair, "Computational fluid dynamic simulation of the supersonic co2 flow during champagne cork popping," Physics of Fluids **34**, 066119 (2022).
[11]G. Liger-Belair, D. Carvajal-Perez, C. Cilindre, J. Facque, M. Brevot, F. Litoux-Desrues, V. Chaperon, and R. Geoffroy, "Evidence for moderate losses of dissolved co2 during aging on lees of a champagne prestige cuvee," Journal of Food Engineering **233**, 40–48 (2018).
[12]L. Wagner, S. Braun, and B. Scheichl, "Simulating the opening of a champagne bottle," Flow **3**, E40 (2023).
[13]K. Soni, D. D. Chandar, and J. Sitaraman, "Development of an overset grid computational fluid dynamics solver on graphical processing units," Computers & fluids **58**, 1–14 (2012).
[14]Z. Gao, Y. Wang, Y. Su, and L. Chen, "Validation of a combined dynamic mesh strategy for the simulation of body's large amplitude motion in wave," Ocean Engineering **187**, 106169 (2019).
[15]H. Schardin, "Die schlierenverfahren und ihre anwendungen," Ergebnisse der exakten Naturwissenschaften , 303–439 (1942).
[16]G. S. Settles, *Schlieren and shadowgraph techniques: visualizing phenomena in transparent media* (Springer Science & Business Media, 2001).
[17]M. J. Hargather and G. S. Settles, "A comparison of three quantitative schlieren techniques," Optics and Lasers in Engineering **50**, 8–17 (2012).
[18]G. S. Settles and M. J. Hargather, "A review of recent developments in schlieren and shadowgraph techniques," Measurement Science and Technology **28**, 042001 (2017).
[19]R. Noll, C. R. Haas, B. Weikl, and G. Herziger, "Computer simulation of schlieren images of rotationally symmetric plasma systems: a simple method," Applied optics **25**, 769–774 (1986).
[20]S. Fu and Y. Wu, "Detection of velocity distribution of a flow field using sequences of schlieren images," Optical Engineering **40**, 1661–1666 (2001).
[21]M. J. Hargather, M. J. Lawson, G. S. Settles, and L. M. Weinstein, "Seedless velocimetry measurements by schlieren image velocimetry," AIAA journal **49**, 611–620 (2011).
[22]J. Schäfer, R. Foest, S. Reuter, T. Kewitz, J. Šperka, and K.-D. Weltmann, "Laser schlieren deflectometry for temperature analysis of filamentary non-thermal atmospheric pressure plasma," Review of Scientific Instruments **83**, 103506 (2012).
[23]R. S. Snedeker *et al.*, "A study of free jet impingement. part 1. mean properties of free and impinging jets," Journal of fluid Mechanics **45**, 281–319 (1971).
[24]P. Lamont and B. Hunt, "The impingement of underexpanded, axisymmetric jets on perpendicular and inclined flat plates," Journal of Fluid Mechanics **100**, 471–511 (1980).
[25]A. Dauptain, L. Gicquel, and S. Moreau, "Large eddy simulation of supersonic impinging jets," AIAA journal **50**, 1560–1574 (2012).
[26]L. Chan, C. Chin, J. Soria, and A. Ooi, "Large eddy simulation and reynolds-averaged navier-stokes calculations of supersonic impinging jets at varying nozzle-to-wall distances and impinging angles," International journal of heat and fluid flow **47**, 31–41 (2014).
[27]A. Sinha and I. Parasuram, "Underexpanded jet impingement on a plane wall—effect of npr and jet standoff distance," in *Conference on Fluid Mechanics and Fluid Power* (Springer, 2021) pp. 13–18.
[28]T. Irie, T. Yasunobu, H. Kashimura, and T. Setoguchi, "Characteristics of the mach disk in the underexpanded jet in which the back pressure continuously changes with time," Journal of Thermal Science **12**, 132–137 (2003).
[29]M. M. Orescanin and J. Austin, "Exhaust of underexpanded jets from finite reservoirs," Journal of Propulsion and Power **26**, 744–753 (2010).
[30]V. Zapryagaev, V. Pickalov, N. Kiselev, and A. Nepomnyashchiy, "Combination interaction of taylor–goertler vortices in a curved shear layer of a supersonic jet," Theoretical and Computational Fluid Dynamics **18**, 301–308 (2004).
[31]Y. Zhu and P. Jiang, "Experimental and numerical investigation of the effect of shock wave characteristics on the ejector performance," International Journal of Refrigeration **40**, 31–42 (2014).
[32]X. Wei, R. Mariani, L. Chua, H. Lim, Z. Lu, Y. Cui, and T. New, "Mitigation of under-expanded supersonic jet noise through stepped nozzles," Journal of Sound and Vibration **459**, 114875 (2019).
[33]K. Tabei, H. Shirai, and F. Takakusagi, "Density measurements of underexpanded free jets of air from circular and square nozzles by means of moire-schlieren method," JSME International Journal **35**, 212–217 (1992).
[34]Y. Otobe, H. Kashimura, S. Matsuo, T. Setoguchi, and H.-D. Kim, "Influence of nozzle geometry on the near-field structure of a highly underexpanded sonic jet," Journal of Fluids and Structures **24**, 281–293 (2008).
[35]A. Bogomolov, A. Roucou, R. Bejjani, M. Herman, N. Moazzen-Ahmadi, and C. Lauzin, "The rotationally resolved symmetric 2oh excitation in h2o-co2 observed using pulsed supersonic expansion and cw-crds," Chemical Physics Letters **774**, 138606 (2021).